nature physics

LETTERS

https://doi.org/10.1038/s41567-019-0631-4

Identification of spin, valley and moiré quasi-angular momentum of interlayer excitons

Chenhao Jin[1,9], Emma C. Regan[1,2,9], Danqing Wang[1,2,9], M. Iqbal Bakti Utama[1,3], Chan-Shan Yang[1,4], Jeffrey Cain[1,5,6], Ying Qin[7], Yuxia Shen[7], Zhiren Zheng[1], Kenji Watanabe[8], Takashi Taniguchi[8], Sefaattin Tongay[7], Alex Zettl[1,5,6] and Feng Wang[1,5,6]*

Moiré superlattices provide a powerful way to engineer the properties of electrons and excitons in two-dimensional van der Waals heterostructures[1–8]. The moiré effect can be especially strong for interlayer excitons, where electrons and holes reside in different layers and can be addressed separately. In particular, it was recently proposed that the moiré superlattice potential not only localizes interlayer exciton states at different superlattice positions, but also hosts an emerging moiré quasi-angular momentum (QAM) that periodically switches the optical selection rules for interlayer excitons at different moiré sites[9,10]. Here, we report the observation of multiple interlayer exciton states coexisting in a WSe_2/WS_2 moiré superlattice and unambiguously determine their spin, valley and moiré QAM through novel resonant optical pump–probe spectroscopy and photoluminescence excitation spectroscopy. We demonstrate that interlayer excitons localized at different moiré sites can exhibit opposite optical selection rules due to the spatially varying moiré QAM. Our observation reveals new opportunities to engineer interlayer exciton states and valley physics with moiré superlattices for optoelectronic and valleytronic applications.

Moiré superlattices between atomically thin materials can dramatically change the properties of electrons and excitons by introducing a new length and energy scale. Artificially stacked moiré superlattices have enabled a variety of intriguing phenomena that are not available in natural systems, such as tunable Mott insulators and unconventional superconductivity[1–8]. At the same time, the large binding energy and long lifetime of interlayer excitons in van der Waals heterostructures have prompted much work on these materials[11,12]. An interlayer exciton is composed of an electron and a hole that are separated in neighbouring layers, so its properties can depend strongly on the layer configurations and external fields. For example, it was recently predicted that moiré superlattices, where the interlayer atomic registry changes periodically over space, can host arrays of localized interlayer exciton states with distinct valley selection rules[9,10]. Therefore, the moiré degree of freedom for interlayer excitons offers exciting opportunities for realizing quantum emitter sources and quantum phases such as the exciton Dirac and Weyl nodes[9,10].

However, direct experimental observation of the interlayer moiré excitons with registration-dependent valley selection rules has been challenging. Because of its sensitivity, photoluminescence has been the only probe used to study interlayer excitons so far. Multiple emission peaks with different optical selection rules have been reported, but interpretation of the photoluminescence spectra is complicated because the photoluminescence intensity is determined by both the oscillator strength and the excited state lifetime and can therefore depend sensitively on a range of sample parameters. Consequently, both the experimental observations and theoretical interpretations vary drastically across different photoluminescence studies[13–17], making it difficult to unambiguously pinpoint the role of a moiré superlattice in the interlayer exciton states. Optical absorption is a more reliable probe of excitons because it directly measures the transition dipole moment, but its application to interlayer excitons has so far been hindered by the small interlayer exciton oscillator strength[18,19]. Here, we overcome this challenge by probing the absorption spectrum of interlayer excitons in near-zero twist angle WSe_2/WS_2 heterostructures with background-free techniques: photoluminescence excitation (PLE) and resonant pump–probe spectroscopy. This combination allows for extremely sensitive measurements of the weak absorption features associated with interlayer moiré excitons, and unambiguously determines the nature of the interlayer excitons, including their relative oscillator strengths and the spin–valley configurations of the constituent electrons and holes. We establish that interlayer excitons with the same spin–valley configuration can have opposite circular selection rules, which is attributed to the different moiré quasi-angular momentum (QAM) associated with the different interlayer lattice registrations. We further show that an opposite-spin exciton state, which was originally forbidden with no valley selectivity, can gain a well-defined circular helicity in the moiré superlattice.

Figure 1a,b presents a schematic and an optical microscope image of a representative near-zero twist angle WSe_2/WS_2 heterostructure (see Methods and ref. [20] for device fabrication details). Figure 1c shows the reflection contrast of the heterostructure in the range of 1.6–2.4 eV. Three prominent absorption peaks are observed around the WSe_2 A exciton energy of 1.7 eV. This is the characteristic behaviour of the intralayer exciton in a moiré superlattice, where the WSe_2 A exciton is split into multiple peaks by the strong moiré superlattice potential[20–22] (see Supplementary Information). The moiré superlattice effects on interlayer excitons are expected to be

[1]Department of Physics, University of California at Berkeley, Berkeley, CA, USA. [2]Graduate Group in Applied Science and Technology, University of California at Berkeley, Berkeley, CA, USA. [3]Department of Materials Science and Engineering, University of California at Berkeley, Berkeley, CA, USA. [4]Institute of Electro-Optical Science and Technology, and Undergraduate Program of Electro-Optical Engineering, National Taiwan Normal University, Taipei, Taiwan. [5]Material Science Division, Lawrence Berkeley National Laboratory, Berkeley, CA, USA. [6]Kavli Energy NanoSciences Institute at University of California Berkeley and Lawrence Berkeley National Laboratory, Berkeley, CA, USA. [7]School for Engineering of Matter, Transport and Energy, Arizona State University, Tempe, AZ, USA. [8]National Institute for Materials Science, Tsukuba, Japan. [9]These authors contributed equally: Chenhao Jin, Emma C. Regan, Danqing Wang. *e-mail: fengwang76@berkeley.edu

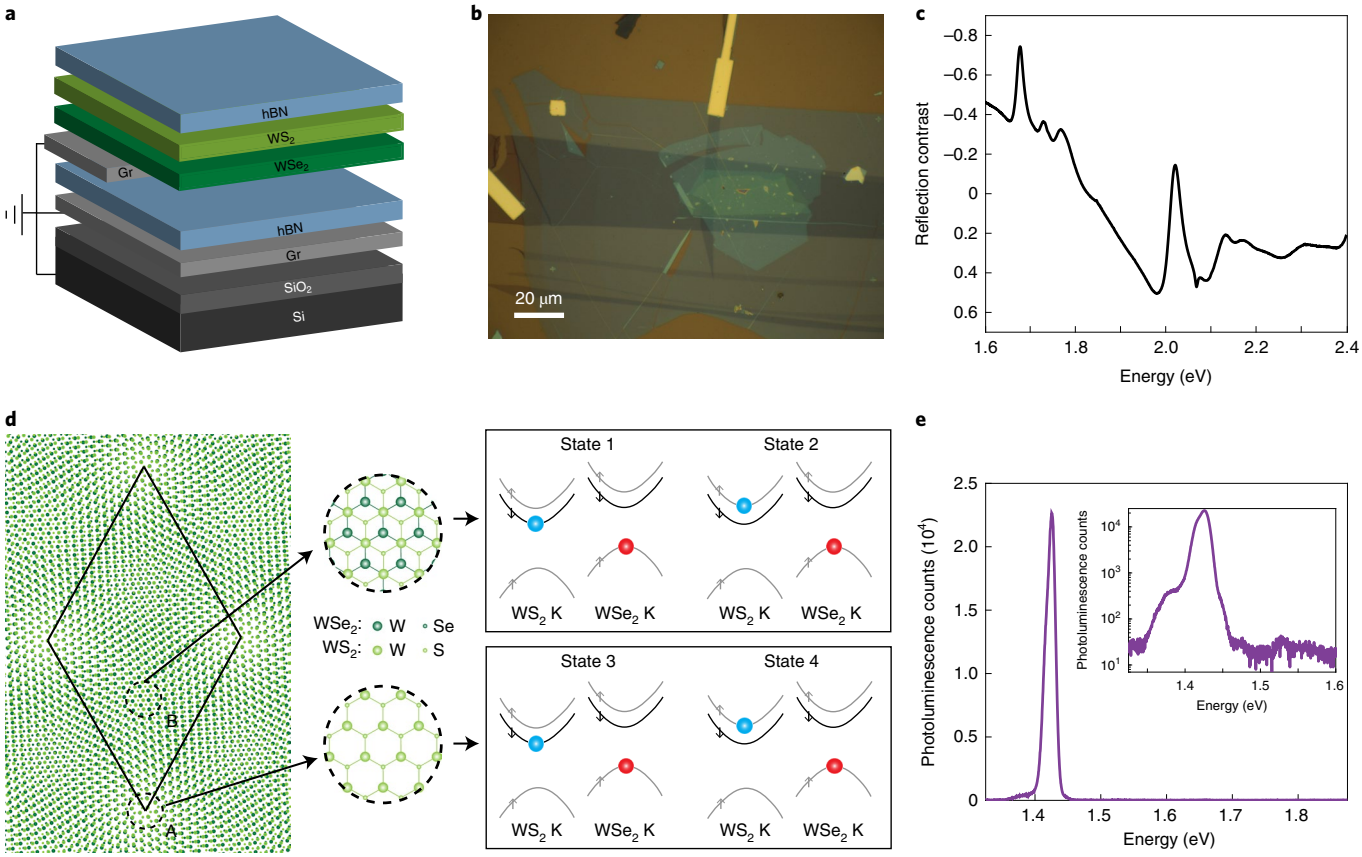

Fig. 1 | Interlayer moiré excitons in near-zero twist angle WSe_2/WS_2 heterostructure. a,**b**, Side-view illustration (**a**) and optical microscope image (**b**) of a representative near-zero twist angle heterostructure. **c**, Reflection contrast of the heterostructure shows three prominent peaks in the WSe_2 A exciton range near 1.7 eV. This is a characteristic absorption signature of the intralayer moiré exciton. **d**, Illustration of the moiré superlattice in real space (left) with the moiré supercell outlined in a black diamond. Interlayer excitons can be trapped at two different local minima of the moiré potential, labelled as A and B points. This moiré degree of freedom, combined with different spin configurations, gives rise to four interlayer exciton states in the K valley (states 1–4 in the boxes to the right). **e**, Photoluminescence spectrum of the heterostructure (log scale in the inset), showing only one prominent peak at 1.43 eV because photoluminescence measurements are only sensitive to the emission state and cannot probe higher-energy states. The much weaker side peak at lower energy may be from defect emission.

even stronger: the interlayer excitons are predicted to localize at different potential minima within the moiré superlattice (labelled as points A and B in Fig. 1d)[9,10]. Consequently, four low-energy interlayer moiré exciton states can exist in the K valley—the same-spin and opposite-spin states centring at the A and B points within the moiré superlattice, respectively. These four states are illustrated in Fig. 1d, and their time-reversal pairs create another set of four states in the K′ valley (not shown).

However, the photoluminescence spectrum of the WSe_2/WS_2 heterostructure shows a single prominent emission peak at 1.43 eV (Fig. 1d), corresponding to only one interlayer exciton state. The much smaller shoulder peak at lower energy (inset, Fig. 1d) may be attributed to defect emission. Although the photoluminescence emission spectrum is extremely sensitive, it is not sufficient to probe different interlayer exciton states or the nature of the interlayer excitons: the lowest energy exciton state, which has the longest population lifetime, can dominate the photoluminescence emission irrespective of its spin or valley characteristics.

We used helicity-resolved PLE spectroscopy to probe higher-energy interlayer moiré exciton states in the WSe_2/WS_2 heterostructure. We monitored both the σ^+- and σ^--polarized photoluminescence emission intensity at 1.43 eV while continuously varying the energy of the excitation photons with σ^+ helicity. Figure 2a,b shows the PLE spectra: the energy of σ^+ excitation light is scanned over the WSe_2 intralayer exciton range (1.65–1.92 eV, Fig. 2a) and interlayer exciton range (1.45–1.55 eV, Fig. 2b). The helicity contrasts for intralayer and interlayer excitation ranges are displayed in Fig. 2c,d, respectively. The photoluminescence emission intensity is proportional to the absorbed photon number and provides a sensitive measurement of the absorption oscillator strength. A strongly enhanced photoluminescence signal is observed when the excitation light is in resonance with the intralayer exciton resonances (Fig. 2a). We also observe well-defined absorption resonances in the interlayer exciton range at 1.46 (green shaded region, Fig. 2b) and 1.51 eV (yellow shaded region). These resonances correspond to two new interlayer moiré exciton states, and their oscillator strengths are more than 100 times smaller than the intralayer exciton transitions. Such weak interlayer exciton transitions are extremely difficult to measure in a direct absorption measurement but are readily observable in the background-free PLE spectroscopy. Furthermore, we observe distinctively different circular helicity behaviours between the intralayer and interlayer excitons: the circular helicity has a large and near-constant value of ~0.5 over the whole intralayer exciton range (Fig. 2c), but changes dramatically and can have opposite signs for different interlayer exciton resonances (Fig. 2d and Supplementary Information).

To resolve the spin and valley properties and to understand the unusual optical selection rules of different interlayer moiré exciton states, we used resonant pump–probe spectroscopy. As illustrated in

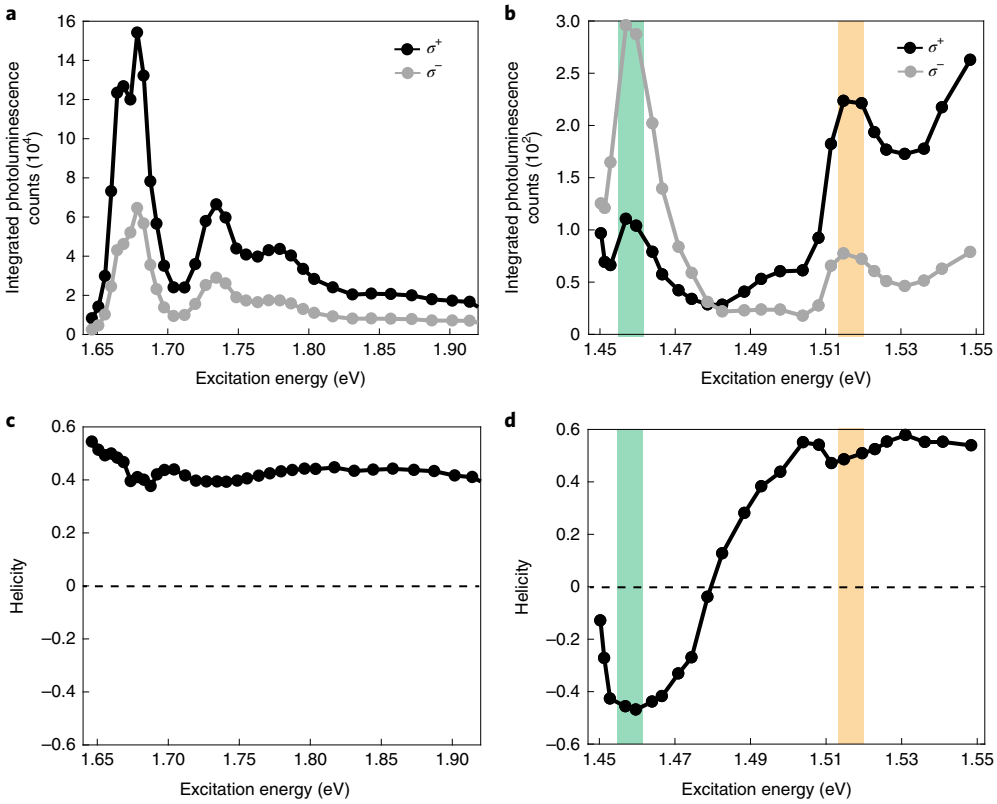

Fig. 2 | Interlayer moiré excitons probed by helicity-resolved PLE spectroscopy. a,**b**, PLE spectra of a representative device measured by monitoring the σ^+ (black) and σ^- (grey) emission intensity of the 1.43 eV emission peak. The energy of σ^+ excitation light is scanned over the intralayer exciton (**a**) and interlayer exciton (**b**) ranges. The emission intensity is strongly enhanced when excitation light is in resonance with all intralayer exciton resonances (**a**) and two additional resonance peaks in the interlayer exciton range (**b**), suggesting the existence of two new interlayer moiré exciton states at 1.46 eV (green shaded area) and 1.51 eV (yellow shaded area), respectively. **c**, Photoluminescence circular helicity shows a near-constant positive value of ~0.5 with intralayer exciton excitation. **d**, Photoluminescence emission shows a circular helicity of ~−0.5 and 0.5 when exciting the 1.46 and 1.51 eV interlayer exciton states, respectively, revealing their unusual optical selection rules. All measurements are performed at 10 K.

Fig. 3a, we resonantly excited an interlayer exciton transition with circularly polarized pump light, and then probed the spin–valley state of the constituent holes in the WSe_2 layer by monitoring the induced absorption changes in the WSe_2 intralayer exciton transitions. This method takes advantage of the fact that the intralayer exciton optical selection rules have already been well established in previous studies[23–25], and they are independent of the relative registration of the two layers[9,10]. Furthermore, the interlayer exciton oscillator strength can be obtained from the signal magnitude of the resonant interlayer-exciton-pump and intralayer-exciton-probe measurements.

Figure 3b shows the pump-induced circular dichroic signal with probe energy fixed at 1.67 eV (near a WSe_2 intralayer exciton feature) and pump energy swept from 1.38 eV to 1.54 eV. Strong pump–probe signals with opposite signs are observed at 1.46 and 1.51 eV (green and yellow shaded regions, respectively). This result reaffirms the PLE observation of two interlayer exciton states at 1.46 and 1.51 eV with different helicity. Interestingly, no clear absorption resonance is observed at the energy of the photoluminescence emission peak (purple shaded region around 1.43 eV). This indicates that the interlayer exciton state that dominates the emission process of the system has small absorption oscillator strength. We label it as a 'weakly absorbing' interlayer exciton state, in contrast to the 'strongly absorbing' states at 1.46 and 1.51 eV.

We resonantly excited the strongly absorbing interlayer exciton states using σ^+ pump light and measured the induced circular dichroic spectra in the WSe_2 intralayer exciton range (Fig. 3c,d). These results can be compared to the pump–probe responses when directly exciting the intralayer exciton at 1.94 eV (Fig. 3e), where the optical selection rule is well established and not affected by the moiré superlattice[9,10]. All three spectral profiles are similar and display prominent resonance features around probe energies of 1.68 and 1.73 eV, corresponding to peaks I and II of the intralayer moiré exciton states in WSe_2, respectively (see Supplementary Information and ref. [20]). This is expected because the pump–probe signals originate from the response of intralayer excitons to valley-polarized holes in WSe_2. However, the sign of the signals is different for the two interlayer exciton states. Pumping at 1.51 eV gives a signal of the same sign as pumping the intralayer exciton. This interlayer exciton state thus has the same optical selection rule as the intralayer exciton so that σ^+ light selectively creates holes in the K valley of WSe_2 (insets of Fig. 3d,e). In contrast, pumping at 1.46 eV gives the opposite sign, indicating that σ^+ light selectively create holes in the K′ valley (inset, Fig. 3c). In other words, the 1.51 and 1.46 eV interlayer exciton states in the K valley will couple more efficiently to σ^+ and σ^- light, and therefore have a total QAM of +1 and −1, respectively (see Supplementary Information).

Based on the spin–valley state of the hole in the WSe_2 layer and the interlayer exciton oscillator strength, we can infer the spin–valley configuration of the electron within the interlayer exciton and determine the emerging moiré QAM, as shown in Table 1. The relatively strong oscillator strengths of the 1.46 and 1.51 eV interlayer exciton states are consistent with theoretical predictions of 'bright' interlayer excitons[19] and require the electron and hole to be in the same valley and of the same spin. Therefore, we can assign a spin contribution of 0 and valley contribution of +1 from the constituent

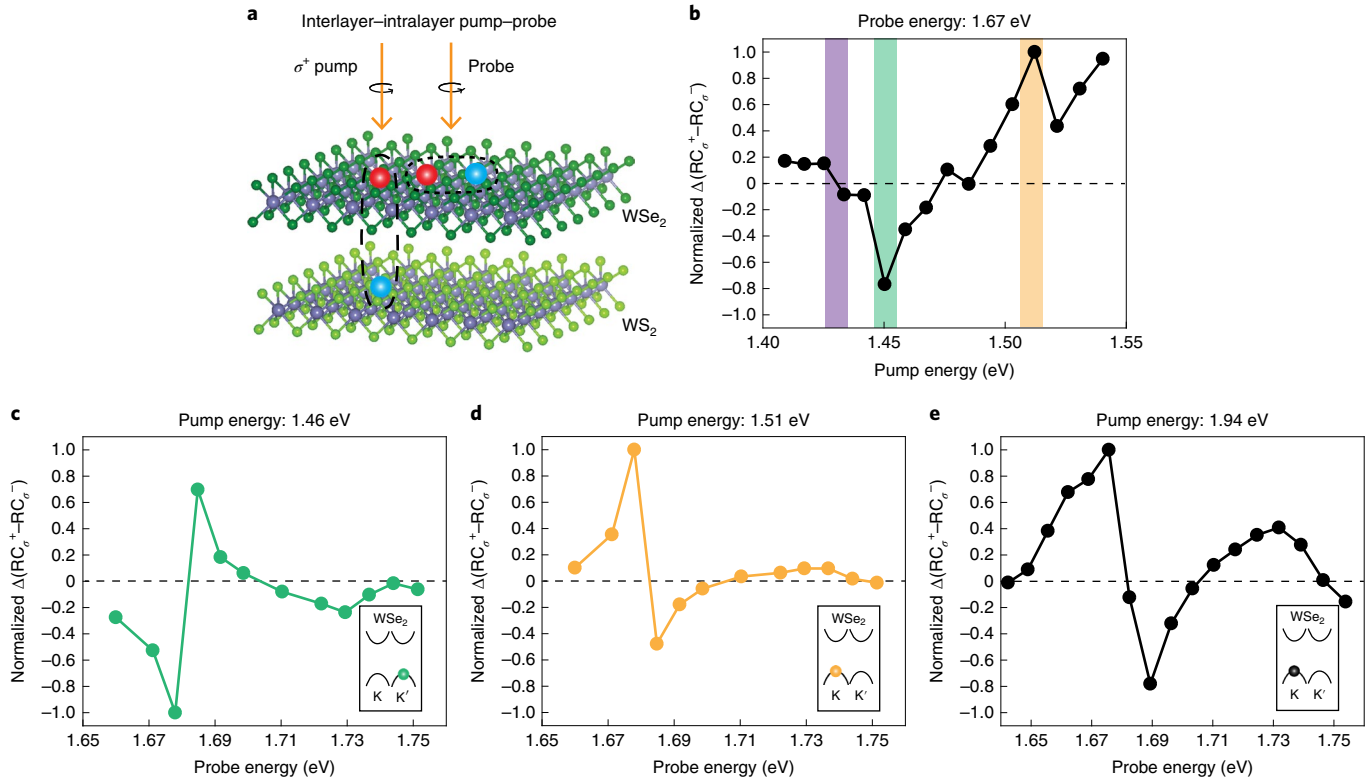

Fig. 3 | Interlayer moiré excitons probed by resonant pump–probe spectroscopy. a, Illustration of the pump–probe experimental design. σ^+ pump light in resonance with an interlayer exciton state directly creates valley-polarized holes in WSe_2, which can then be probed by the induced circular dichroic signal at the WSe_2 intralayer exciton energy. **b**, Pump-induced circular dichroic signal with probe energy fixed at 1.67 eV and pump energy swept from 1.38 eV to 1.54 eV. The two prominent resonances with opposite sign at 1.46 eV (green shaded region) and 1.51 eV (yellow shaded region) reaffirm the two interlayer moiré exciton states observed in PLE measurements. The 1.43 eV state, on the other hand, shows no clear resonance (purple shaded region), indicating its weakly absorbing nature. RC, reflection contrast. **c**–**e**, Pump-induced circular dichroic spectra with pump energy in resonance with the 1.46 eV state (**c**) and 1.51 eV state (**d**), and in the intralayer exciton range at 1.94 eV (**e**). The circular dichroic spectra when pumping the 1.51 eV interlayer exciton state gives the same sign as when pumping the intralayer exciton, so in both cases the σ^+ pump create holes in the K valley of WSe_2 (insets of **d** and **e**). In contrast, an opposite sign is observed when pumping the 1.46 eV state, indicating that σ^+ light selectively create holes in the K′ valley (inset of **c**). All measurements are performed at 10 K.

Table 1 | The nature of different interlayer moiré exciton states and the spin, valley and moiré contributions to their optical selection rules

	Experimental results				Inferred conclusions				
State	Energy (eV)	Oscillator strength	Total QAM	Hole valley and spin	Electron valley and spin	Spin QAM	Valley QAM	Moiré QAM	Moiré position
1	1.43	Weak	+1=−2	K ↑	K↓	−1	+1	−2	B
2	1.46	Strong	−1	K ↑	K ↑	0	+1	−2	B
3		Not observed	0	K ↑	K ↓	−1	+1	0	A
4	1.51	Strong	+1	K ↑	K ↑	0	+1	0	A
5	1.43	Weak	−1=+2	K′ ↓	K′ ↑	1	−1	+2	B
6	1.46	Strong	+1	K′ ↓	K′ ↓	0	−1	+2	B
7		Not observed	0	K′ ↓	K′ ↑	1	−1	0	A
8	1.51	Strong	−1	K′ ↓	K′ ↓	0	−1	0	A

electron and hole to the QAM of the K-valley interlayer exciton (see Supplementary Information). The rest of the contribution to the QAM arises from the local interlayer atomic registry in the moiré superlattice. Consequently, we determine a moiré QAM of −2 for the 1.46 eV interlayer exciton and zero for the 1.51 eV interlayer exciton. They correspond to the second (moiré position B) and fourth (moiré position A) state illustrated in Fig. 1d, respectively.

The lowest-energy interlayer exciton state at 1.43 eV has weak oscillator strength, and we attribute this to an interlayer exciton with opposite electron and hole spin based on the electronic bands of the heterostructure (Fig. 1d). This arises naturally because the spin–orbital coupling has opposite sign in the conduction and valence bands for W-based transition metal dichalcogenide materials[26,27]. This opposite spin state is not completely dark, because spin is no longer a good

quantum number in systems with strong spin–orbital coupling[28–30]. The observed energy separation between the opposite- and same-spin interlayer excitons (state 1 and 2) is ~30 meV, which is consistent with the known conduction band spin splitting in WS_2 layers[26,27]. Previously, an intralayer opposite-spin exciton has been observed in the photoluminescence emission of monolayer WSe_2 without a magnetic field[31,32], but it shows no circular valley selection, as its QAM only comes from the spin–valley contribution and is 0 (refs. [28,29]). In contrast, emission from the 1.43 eV interlayer exciton state shows a large σ^+ circular helicity when we excite intralayer excitons with σ^+-polarized light (Fig. 2b). This indicates that the lowest-energy K-valley interlayer exciton has a total QAM of +1 (state 1, Fig. 1d). This again highlights the important role of the moiré superlattice, which introduces an additional QAM of +1 (or equivalently, −2, due to the three-fold rotation symmetry in the system) and a well-defined circular selection rule to the lowest-energy opposite-spin state. The other opposite-spin state—state 3—is not observed in our study, presumably due to its very small oscillator strength. The spin, valley and moiré configurations of different interlayer moiré exciton states and their respective valley selection rules in Table 1 match very well with a recent theoretical study[33], further justifying our assignments.

Combining the ability to engineer spin–valley selection rules using the moiré degree of freedom, the coexistence of multiple moiré states with distinctively different optical properties and the tunability from the layer configuration and external fields, interlayer excitons in the WSe_2/WS_2 moiré superlattice provide a versatile platform for exciting new exciton and valley physics.

Online content

Any methods, additional references, Nature Research reporting summaries, source data, statements of code and data availability and associated accession codes are available at https://doi.org/10.1038/s41567-019-0631-4.

Received: 15 February 2019; Accepted: 8 July 2019;
Published online: 26 August 2019

References

1. Cao, Y. et al. Unconventional superconductivity in magic-angle graphene superlattices. *Nature* **556**, 43–50 (2018).
2. Cao, Y. et al. Correlated insulator behaviour at half-filling in magic-angle graphene superlattices. *Nature* **556**, 80–84 (2018).
3. Chen, G. R. et al. Evidence of a gate-tunable Mott insulator in a trilayer graphene moire superlattice. *Nat. Phys.* **15**, 237–241 (2019).
4. Spanton, E. M. et al. Observation of fractional Chern insulators in a van der Waals heterostructure. *Science* **360**, 62–66 (2018).
5. Wallbank, J. R., Patel, A. A., Mucha-Kruczynski, M., Geim, A. K. & Falko, V. I. Generic miniband structure of graphene on a hexagonal substrate. *Phys. Rev. B* **87**, 245408 (2013).
6. Song, J. C. W., Samutpraphoot, P. & Levitov, L. S. Topological Bloch bands in graphene superlattices. *Proc. Natl Acad. Sci. USA* **112**, 10879–10883 (2015).
7. Gorbachev, R. V. et al. Detecting topological currents in graphene superlattices. *Science* **346**, 448–451 (2014).
8. Lee, M. et al. Ballistic miniband conduction in a graphene superlattice. *Science* **353**, 1526–1529 (2016).
9. Yu, H. Y., Liu, G. B., Tang, J. J., Xu, X. D. & Yao, W. Moiré excitons: from programmable quantum emitter arrays to spin–orbit-coupled artificial lattices. *Sci. Adv.* **3**, e1701696 (2017).
10. Wu, F. C., Lovorn, T. & MacDonald, A. H. Theory of optical absorption by interlayer excitons in transition metal dichalcogenide heterobilayers. *Phys. Rev. B* **97**, 035306 (2018).
11. Rivera, P. et al. Observation of long-lived interlayer excitons in monolayer $MoSe_2$–WSe_2 heterostructures. *Nat. Commun.* **6**, 6242 (2015).
12. Latini, S., Winther, K. T., Olsen, T. & Thygesen, K. S. Interlayer excitons and band alignment in MoS_2/hBN/WSe_2 van der Waals heterostructures. *Nano Lett.* **17**, 938–945 (2017).
13. Hsu, W. T. et al. Negative circular polarization emissions from WSe_2/$MoSe_2$ commensurate heterobilayers. *Nat. Commun.* **9**, 1356 (2018).
14. Hanbicki, A. T. et al. Double indirect interlayer exciton in a $MoSe_2$/WSe_2 van der Waals heterostructure. *ACS Nano* **12**, 4719–4726 (2018).
15. Tran, K. et al. Evidence for moiré excitons in van der Waals heterostructures. *Nature* **567**, 71–75 (2019).
16. Seyler, K. L. et al. Signatures of moiré-trapped valley excitons in $MoSe_2$/WSe_2 heterobilayers. *Nature* **567**, 66–70 (2019).
17. Ciarrocchi, A. et al. Polarization switching and electrical control of interlayer excitons in two-dimensional van der Waals heterostructures. *Nat. Photon.* **13**, 131–136 (2019).
18. Ross, J. S. et al. Interlayer exciton optoelectronics in a 2D heterostructure p–n junction. *Nano Lett.* **17**, 638–643 (2017).
19. Gillen, R. & Maultzsch, J. Interlayer excitons in $MoSe_2$/WSe_2 heterostructures from first principles. *Phys. Rev. B* **97**, 165306 (2018).
20. Jin, C. H. et al. Observation of moire excitons in WSe_2/WS_2 heterostructure superlattices. *Nature* **567**, 76–80 (2019).
21. Wu, F. C., Lovorn, T. & MacDonald, A. H. Topological exciton bands in moire heterojunctions. *Phys. Rev. Lett.* **118**, 147401 (2017).
22. Zhang, N. et al. Moiré intralayer excitons in a $MoSe_2$/MoS_2 heterostructure. *Nano Lett.* **18**, 7651–7657 (2018).
23. Cao, T. et al. Valley-selective circular dichroism of monolayer molybdenum disulphide. *Nat. Commun.* **3**, 887 (2012).
24. Mak, K. F., He, K., Shan, J. & Heinz, T. F. Control of valley polarization in monolayer MoS_2 by optical helicity. *Nat. Nanotechnol.* **7**, 494–498 (2012).
25. Xiao, D., Liu, G.-B., Feng, W., Xu, X. & Yao, W. Coupled spin and valley physics in monolayers of MoS_2 and other group-VI dichalcogenides. *Phys. Rev. Lett.* **108**, 196802 (2012).
26. Andor, K. et al. k·p theory for two-dimensional transition metal dichalcogenide semiconductors. *2D Mater.* **2**, 022001 (2015).
27. Zhang, X.-X., You, Y., Zhao, S. Y. F. & Heinz, T. F. Experimental evidence for dark excitons in monolayer WSe_2. *Phys. Rev. Lett.* **115**, 257403 (2015).
28. Wang, G. et al. In-plane propagation of light in transition metal dichalcogenide monolayers: optical selection rules. *Phys. Rev. Lett.* **119**, 047401 (2017).
29. Echeverry, J. P., Urbaszek, B., Amand, T., Marie, X. & Gerber, I. C. Splitting between bright and dark excitons in transition metal dichalcogenide monolayers. *Phys. Rev. B* **93**, 121107 (2016).
30. Zhou, Y. et al. Probing dark excitons in atomically thin semiconductors via near-field coupling to surface plasmon polaritons. *Nat. Nanotechnol.* **12**, 856–860 (2017).
31. Li, Z. P. et al. Revealing the biexciton and trion-exciton complexes in BN encapsulated WSe_2. *Nat. Commun.* **9**, 3719 (2018).
32. Chen, S. Y., Goldstein, T., Taniguchi, T., Watanabe, K. & Yan, J. Coulomb-bound four- and five-particle intervalley states in an atomically-thin semiconductor. *Nat. Commun.* **9**, 3717 (2018).
33. Yu, H. Y., Liu, G. B. & Yao, W. Brightened spin–triplet interlayer excitons and optical selection rules in van der Waals heterobilayers. *2D Mater.* **5**, 035021 (2018).

Acknowledgements

This work was supported primarily by the US Department of Energy, Office of Science, Office of Basic Energy Sciences, Materials Sciences and Engineering Division under contract no. DE-AC02-05-CH11231 (van der Waals heterostructures program, KCWF16). PLE spectroscopy of the heterostructure is supported by the US Army Research Office under MURI award W911NF-17-1-0312. The growth of hBN crystals was supported by the Elemental Strategy Initiative conducted by the MEXT, Japan and JSPS KAKENHI grant no. JP15K21722. S.T. acknowledges support from an NSF DMR 1552220 NSF CAREER award for the growth of WS_2 and WSe_2 crystals. E.C.R. acknowledges support from the Department of Defense (DoD) through the National Defense Science & Engineering Graduate Fellowship (NDSEG) Program. C.-S.Y. acknowledges support from grant no. 107-2112-M-003-014-MY3 from the Ministry of Science and Technology.

Author contributions

F.W. and C.J. conceived the research. C.J., E.C.R. and C.-S.Y. built the optical set-up. C.J., E.C.R. and D.W. carried out optical measurements. C.J., F.W. and E.C.R. performed theoretical analysis. E.C.R., D.W., M.I.B.U. and Z.Z. fabricated van der Waals heterostructures. Y.Q., Y.S., S.T., J.C. and A.Z. grew the WSe_2 and WS_2 crystals. K.W. and T.T. grew the hBN crystals. All authors discussed the results and wrote the manuscript.

Competing interests

The authors declare no competing interests.

Additional information

Supplementary information is available for this paper at https://doi.org/10.1038/s41567-019-0631-4.

Reprints and permissions information is available at www.nature.com/reprints.

Correspondence and requests for materials should be addressed to F.W.

Peer review information: *Nature Physics* thanks Paulina Plochocka, Jun Yan and Ziliang Ye for their contribution to the peer review of this work.

Publisher's note: Springer Nature remains neutral with regard to jurisdictional claims in published maps and institutional affiliations.

Methods

Heterostructure preparation. Monolayer WSe_2, monolayer WS_2, few-layer graphene and thin hexagonal boron nitride (hBN) flakes were exfoliated onto silicon substrates with a 90 nm silicon oxide layer. Polarization-dependent second harmonic generation (SHG) was used to determine the relative angles between the WSe_2 and WS_2 crystalline axes (see Supplementary Information and ref. [20]). The WSe_2/WS_2 heterostructures were prepared using a dry transfer method with a polyethylene terephthalate (PET) stamp[34]. A PET stamp was used to pick up the top hBN flake, the WS_2 monolayer, the WSe_2 monolayer, a few-layer graphene electrode, the bottom hBN and the few-layer graphene back gate at 60 °C. The angle of the PET stamp was adjusted manually between picking up the WS_2 and WSe_2 flakes to ensure that the angle between the crystal axes was near zero. The PET stamp was then stamped onto a clean Si substrate with 90 nm SiO_2 at 130 °C, and the PET was dissolved in dichloromethane for 12 h at room temperature. Contacts (~75 nm gold with ~5 nm chromium adhesion layer) to the few-layer graphene flakes were made using electron-beam lithography and electron-beam evaporation.

PLE spectroscopy. PLE measurements were performed using a pulsed supercontinuum laser source (Fianium FemtoPower 1060), which was spectrally filtered by a grating and appropriate filters to provide a tunable excitation light with 0.3 nm linewidth. The σ^+ polarization state of the excitation beam was set with a linear polarizer and quarter wave plate. The excitation light was focused at the sample with ~3 μm beam size. σ^+- and σ^--polarized photoluminescence was collected at each excitation energy and analysed with a monochromator and a liquid-nitrogen-cooled charge coupled device. The photoluminescence spectra were normalized to the excitation power and integration time. We verified that the photoluminescence intensity scaled linearly with excitation power for all energies studied. The integrated photoluminescence peak intensity was then plotted as a function of the excitation energy.

Resonant pump–probe spectroscopy. Femtosecond pulses at 1,026 nm (repetition rate of 150 kHz and duration of ~300 fs) were generated by a regenerative amplifier seeded by a mode-locked oscillator (Light Conversion PHAROS). The femtosecond pulses were split into two paths. One was used to pump an optical parametric amplifier (Light Conversion TOPAS). Its signal output was then used as the pump light in our measurement. The second portion of the 1,026 nm beam was focused onto a sapphire crystal to generate broadband white light, which was then spectrally filtered by appropriate bandpass filters (each with 10 nm full-width at half-maximum) to serve as the probe light. The pump and probe polarizations were set with linear polarizers and a shared quarter wave plate. The pump–probe delay time was controlled with a motorized delay stage. The pump and probe beams were focused at the sample with diameters of 50 μm and 25 μm, respectively. The reflected probe light was detected by a photomultiplier tube after wavelength selection using a monochromator (passing bandwidth of 5 nm). The pump–probe signal was analysed using a lock-in amplifier at ~2.5 kHz modulation frequency.

Data availability

The data that support the findings of this study are available from the corresponding author upon reasonable request.

References

34. Wang, L. et al. One-dimensional electrical contact to a two-dimensional material. *Science* **342**, 614–617 (2013).